J Solid State Electrochem (2010) 14:1177–1184
DOI 10.1007/s10008-009-0942-y

ORIGINAL PAPER

Morphology-to-properties correlations in anodic porous InP layers

Lionel Santinacci · Anne-Marie Gonçalves · Muriel Bouttemy · Arnaud Etcheberry

Received: 21 July 2009 / Revised: 22 September 2009 / Accepted: 24 September 2009 / Published online: 10 October 2009
© Springer-Verlag 2009

Abstract In this paper, we investigate the properties of porous structures anodically grown onto n-InP (100) in HCl. In situ electrochemical characterizations show the pore morphology strongly influences the properties of the InP surfaces. Both dc- and ac-electrochemical measurements reveal an enhancement of the capacitive current and a modification of the electronic distribution at the interface. Photocurrent spectra performed during the pore growth are also strongly modified. For low anodic charges, an increase of the photocurrent with a redshift of the absorption edge is measured. These evolutions can be respectively ascribed (*i*) to a reflection decrease due to a surface roughening and (*ii*) to the creation of surface states within the band gap. For higher anodic charges, the photocurrent drops with a narrowing of the spectrum. Using a model based on the "dead" layer, the porous layer is considered as an absorbent film that progressively attenuates the photocurrent of the bulk semiconductor.

Keywords III–V semiconductors · Porous materials · Anodic films · Nanostructured materials

Introduction

Similarly to other one-dimensional nanostructures, the specific properties of porous semiconductors are directly related to their peculiar geometry (for a review, see, e.g., [1]). It is therefore crucial to control and tailor the pore morphology by adjusting parameters such as the electrochemical conditions, the electrolyte composition, the doping (density and type), and the crystal orientation. In addition to its evident optoelectronic properties, InP exhibits a wide panel of pore morphologies. Macropores have been firstly grown onto InP by photoetching in 1983 [2], while mesopores were reported by Takizawa et al. [3] 10 years later. Finally, it is Föll's group who gave a detailed description of the numerous pore morphologies obtained on this semiconductor [4]. For low applied current densities, the dissolution proceeds preferentially along the ⟨111⟩ directions (crystal-oriented or CO pores), whereas current line oriented (CLO) pores are grown perpendicularly to the surface for high currents [5]. For very high current densities, self-induced voltage oscillations correlated to periodic variations of the pore diameter have also been observed [6], and under potentiostatic control, it is possible to etch uniform perpendicular pores that can be self-organized according to a hexagonal network [7]. Although halogenic acids such as HCl, HBr, and HF are often used [8], different geometries (e.g., square-shaped or coral-like pores) have been fabricated in other aqueous solutions such as HCl/HNO_3, $HCl/H_2PtCl_6/NH_4OH$, KOH [9, 10], or, more recently, in non-aqueous solvents such as liquid ammonia [11] or dimethylformamide [12].

Holes (h^+) are required to perform anodic dissolution of semiconductors. Since they are the minority carriers in n-type material, the charge transfer occurs therefore either by avalanche or tunneling breakdown, and the pore wall thickness (t_p) corresponds roughly to double the width (W) of the space charge layer

L. Santinacci (✉) · A.-M. Gonçalves · M. Bouttemy · A. Etcheberry
Institut Lavoisier de Versailles (UMR 8180),
Université de Versailles Saint Quentin - CNRS,
45 avenue des Etats-Unis, 78035 Versailles cedex, France
e-mail: lionel.santinacci@uvsq.fr

(SCL). It appears, therefore, that the charge distribution in the pore walls strongly differs from that of the flat surface. The electric and optical properties should thus be modified according to the geometry of the nanowalls. Such morphology-to-properties correlations have been reported and are still investigated for a wide range of one-dimensional nanostructures. Due to the high area of the porous structures (A_p), an apparent enhancement of the interfacial capacitance (C) occurs during the porous etching. Peter et al. have reported an enlargement of Helmholtz's double-layer capacitance (C_H) by cyclic voltammetry performed on Si during the pore growth [13], and other authors have used electrochemical impedance during porous etching onto GaP and SiC to measure the steep increase of the SCL's capacitance (C_{sc}) [14, 15]. The photocurrent (j_{ph}) characteristics of porous semiconductors can also exhibit significant variations caused by their own geometry. Both j_{ph} enhancement (e.g., for indirect band gap semiconductors such as GaP and SiC [15, 16]) and quenching (e.g., for CdZnTe [17]) have been reported. In the first case, the j_{ph} expansion is ascribed to the enlarged light scattering within the porous structures inducing a better photon absorption, whereas, in the second case, the j_{ph} decrease corresponds to better charge recombinations in the pore walls.

In a previous paper, photoluminescence quenching has been evidenced, ex situ, for porous layers formed in acidic liquid ammonia [11]. Here, porous films anodically grown onto n-InP (100) in HCl are characterized by several in situ methods in order to correlate the measured properties to the features' morphology. Scanning electron microscopy (SEM) was used to observe the pore geometry and to determine growth rate while (photo-)electrochemical techniques, such as cyclic voltammetry, capacitance measurements, and photocurrent spectroscopy, have been used to describe the charge distribution at the porous semiconductor/electrolyte interface during the initiation phase and the growth regime. The correlations between the observed pore geometry and the modified properties of the etched surfaces are established, compared to literature, and discussed.

Experimental

Samples used to perform the porous etching were Sn doped n-InP (100) from InPACT ($N_D = 1$ to 2×10^{18} at per cubic centimeter). The wafers were cleaved into square-pieces of 4×4 mm^2 and were cleaned with methanol. Ohmic backcontact to the electrodes was established by smearing in and annealing it under H_2 stream at $T = 380°C$.

Porous etching and electrochemical characterizations were carried out using a three electrode configuration. A 1 M KCl silver/silver chloride electrode ($E^{\circ} =$ 199 mV vs SHE) and a Pt wire served, respectively, as reference and counter electrodes. The electrochemical cell was placed in the dark and was connected to a PARSTAT 2263 potentiostat/galvanostat. Porous layers were formed by galvanic steps in 1 M HCl at $j = 100\,\mathrm{mA\,cm^{-2}}$. Cyclic voltammetry was performed, during the porous etching, in the dark or under white light illumination using an Oriel 6135 W/Xe 250 W lamp. The scanning rate (υ) was 20 mV s^{-1} unless otherwise mentioned in the text. Capacitance measurements were performed during the anodic porous etching using the same equipment with a constant frequency ($f = 11$ kHz) and a perturbation amplitude of 10 mV. Each capacitance measurement takes approximately 30 s. Both currents and capacitances are normalized by the initial nominal area of the electrode ($A_{\circ}$). The additional area induced by the porous etching is not taken into account.

Low-level photocurrent spectroscopy was achieved between successive porous etching steps. The beam coming out of the lamp was attenuated by an optical filter in order to limit the anodic photocurrent as much as possible. The incident white light was monochromated and chopped using a Jobin Yvon HR 320 monochromator and a Bentham 218 chopper coupled to an EG&G 5208 lock-in amplifier and a PAR 273 potentiostat. The photocurrent intensity was corrected using a Si photodiode (UDT-OSI Optoletronics). The scanning of the wavelength (λ) from 600 to 1,000 nm takes 144 s long. The pore morphology was investigated by SEM using a Hitachi S4800 high resolution microscope.

Results and discussion

Pore morphology

Figure 1 shows a SEM cross section of a porous layer grown onto a n-InP surface at 100 mA cm^{-2} for 60 s. According to literature [5], CLO pores are expected to grow. Here, the pores exhibit an almost CLO geometry, i.e., channels perpendicular to the surface showing diameter variations due to some CO etching features (see inset in Fig. 1). It indicates the applied current is sufficiently high to generate the perpendicular etching but not enough to get fully rid of the preferential dissolution along the ⟨111⟩ directions. Using a higher current density or a higher dopant concentration would remove

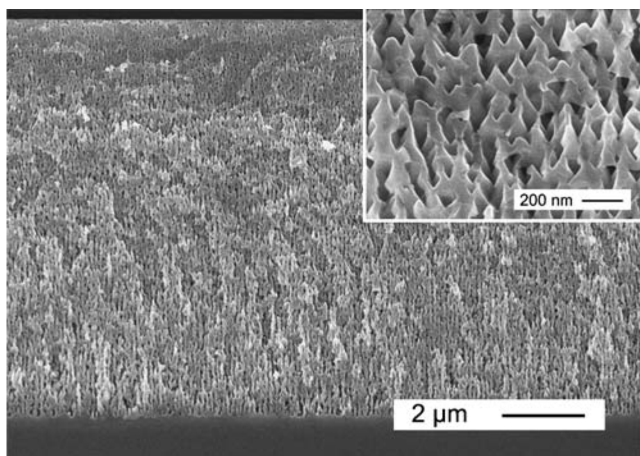

Fig. 1 SEM cross section of a porous n-InP layer grown in 1 M HCl at 100 mA cm^{-2} for 60 s ($Q = 6$ C cm^{-2}). *Inset*: high-magnification SEM cross section

these crystallographic features. Note that almost no synchronized size fluctuations related to potential (U) oscillations are observed. Such a phenomenon occurs for longer polarization times, i.e., for higher anodic charges ($Q \geq 7$ C cm^{-2}). Although the pore geometry is not perfectly regular and uniform, averaged dimensions can roughly be estimated from the SEM observations. The typical radius (r_p) of the etch channels varies between 25 and 50 nm, the wall thickness (t_p) is in the 50 to 100 nm range, and the pore density (N_p) is roughly $6.5 \pm 1 \times 10^9$ cm^{-2}. The depth of the film (d_p) is plotted against the anodic charge in Fig. 2. As seen on the plot, the pore depth evolves linearly with the charge ($d_p = k \times Q$). The slope (k) corresponds, therefore, to the growth rate and is roughly equal to 1.6 μm/C cm^{-2}. Although some triangular etching features are present,

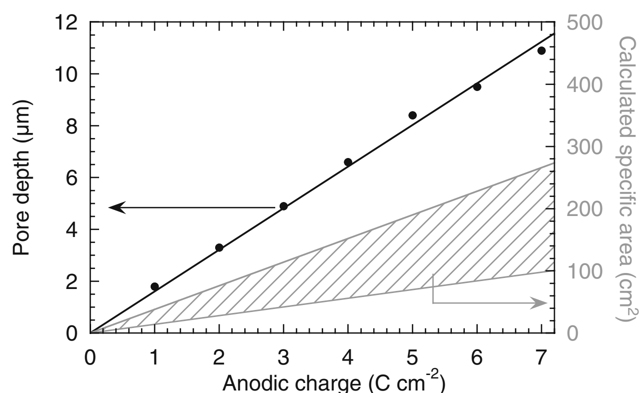

Fig. 2 Evolution of the pore depth with the charge passed during the porous etching (*circles*). *Cross-hatched zone* corresponds to the range of the porous area calculated according to Eq. 1 with respect to the inaccuracy on r_p and N_p

the pores exhibit a global tubular morphology. To simplify the calculation of the area in the porous layer with a reasonable precision, the range of A_p is estimated using a cylindrical geometry:

$$A_p = 2\pi r_p \cdot N_p \cdot d_p \tag{1}$$

Since the pore depth is proportional to the anodic charge, Eq. 1 can be rewritten as Eq. 2:

$$A_p = 2\pi r_p \cdot N_p \cdot k \cdot Q \tag{2}$$

Thus, A_p is directly proportional to the passed charge and can be calculated with respect to the relatively high inaccuracy on r_p and N_p. The range of A_p is therefore plotted against Q in Fig. 2. According to this calculation, the electrode area is drastically increased during the porous etching. A_p is indeed strongly expanded since one observes $100 \times A_\circ < A_p < 300 \times A_\circ$ after passing 7 C cm^{-2}. Such A_p variation will be discussed in the following section with regard to the electrochemical response of the porous surface.

Electrochemical characterizations

Cyclic voltammetry

Electrochemical characterizations of the porous layer have been performed by both dc and ac methods. Figure 3a shows the typical current–voltage curve of a flat n-InP electrode immersed in 1 M HCl in dark conditions (black line). The curve exhibits the typical rectifying behavior of a n-type semiconductor/electrolyte junction. Almost no current flows through the interface for voltages positive to the flat band potential ($U_{fb} = -0.6$ V, determined from Fig. 5), and a metallic behavior is observed for potentials more negative than U_{fb}. The onset for H^+ reduction appears around −0.6 V since the Schottky barrier is low for electrons while the anodic current observed at high positive overvoltages (ca. 0.6 V) corresponds to the material dissolution occurring when the junction breakdown is reached.

After pore formation, the current response is enhanced because the working area of the electrode is increased (gray line). The onset for H^+ reduction appears, therefore, at a less cathodic overvoltage while no strong variations are observed on the anodic branch at 0.6 V (Fig. 3a). Figure 3c presents an enlarged view of the initial current–voltage response of the electrode (black line) and a series of voltammograms (gray lines) measured after porous etching ($Q = 4$ C cm^{-2}) for an increasing scanning rate. The potential range has been reduced to −0.06 to 0.14 V to avoid the faradic contributions to the measured current as much as possible.

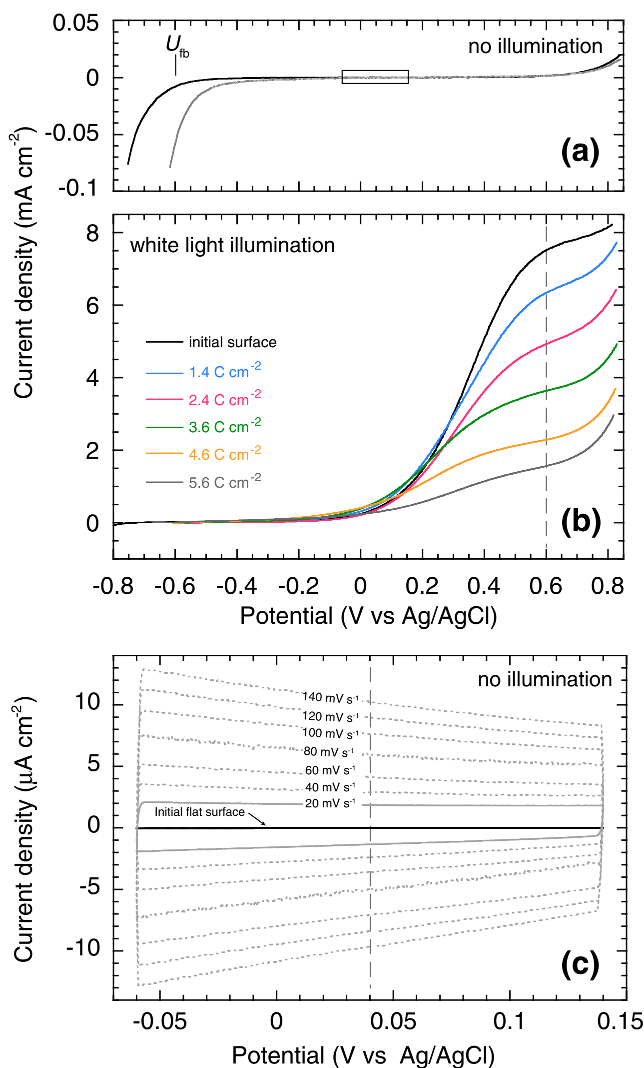

Fig. 3 Cyclic voltammograms of n-InP in 1 M HCl ($v = 20\,\mathrm{mV\,s^{-1}}$). **a** Initial surface (*black line*) and porous surface after passing $2\,\mathrm{C\,cm^{-2}}$ (*gray*) without illumination. The *rectangle* corresponds to the potential range shown in **c**. **b** Sample under white light illumination after successive porous etching steps. The *vertical dashed line*, located at $U = 0.6\,\mathrm{V}$, refers to Fig. 6. **c** Initial surface (*black*) and porous surface after passing $4\,\mathrm{C\,cm^{-2}}$ (*gray*) without illumination. Influence of the v for the porous surface (*gray dotted lines*). The *vertical dashed line*, located at $U = 0.04\,\mathrm{V}$, refers to the next figure

After passing an anodic charge of $4\,\mathrm{C\,cm^{-2}}$, the surface exhibits an enhanced current (gray full line). The cyclic voltammogram is almost rectangular on the whole potential range and a progressive enlargement of this rectangular-shaped voltammogram is observed when the scanning rate is stepped up (gray dotted lines). This evolution suggests an increase of the capacitive contribution of the current. The cathodic and anodic currents (j_c and j_a, respectively) measured at $U = 0.04$ V (see the vertical dashed line on Fig. 3c) are plotted against the scanning rate in Fig. 4a. The linear behaviors of j_c and j_a are expected since, according to Eq. 3, capacitive currents correspond to the charging of the interfacial capacitance and should be proportional to v and C. Thus, the interfacial capacitance is deduced from the slopes of j_c and j_a vs v (here, for $Q = 4\,\mathrm{C\ cm^{-2}}$, $C = 65\ \mu\mathrm{F\ cm^{-2}}$).

$$j = C \cdot \left(\frac{\mathrm{d}V}{\mathrm{d}t}\right), \qquad \text{here} \quad |j| = C \cdot v \tag{3}$$

The evolution of the anodic current measured on different samples after porous etching with an increasing anodic charge is plotted on Fig. 4b. Again, the current exhibits a linear dependency on Q since, according to Eq. 4, the capacitance increases linearly with the electrode area (A):

$$C = \frac{\epsilon\epsilon_o}{s} \cdot A \qquad \text{with} \quad A \propto Q, \tag{4}$$

where s, ϵ, and ϵ_o correspond to the separation of the plates (usually $s = 5\,\text{Å}$ in Helmholtz's double layer), the dielectric constant of the medium, and the permittivity of vacuum, respectively. The linear evolutions of the j with v and Q show the capacitive nature of the current measured on the porous electrode. Thus, after passing an anodic charge of $4\,\mathrm{C\ cm^{-2}}$, the relative increase of the area (A'_p) can be deduced: $130\,\mathrm{cm^2}$. On one hand, it has been shown in Fig. 2 that the working area of the electrode is proportional to Q (Eq. 2) and, on the other hand, Eqs. 3 and 4 correlate the current, the capacitance, and the area. The comparison of the variations A_p with C during the porous etching indicates consistent evolutions. The determination of the relative evolution of A'_p using Eqs. 3 and 4 with the experimental values of C is indeed in good agreement with A_p calculated from the cylindrical description of

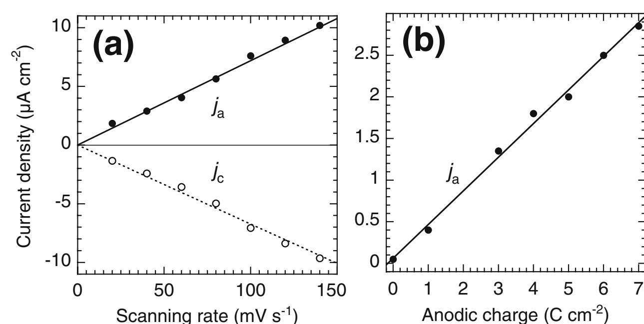

Fig. 4 **a** Anodic and cathodic currents plotted against the scanning rate after passing $4\,\mathrm{C\,cm^{-2}}$ (j_c and j_a are measured at 0.04 V on Fig. 3). **b** Anodic current density vs charge on various samples ($U = 0.1$ V and $v = 20\,\mathrm{mV\,s^{-1}}$)

the pores (plotted in Fig. 2) since one found $14 \times Q \leq A_p \leq 38 \times Q$ in the first case and $A'_p \approx 33 \times Q$ in the second.

The slopes of $|j_c|$ and $|j_a|$ against the scanning rate are similar. Using Eq. 3, they give the interfacial capacitance of the initial flat surface ($C = 0.5 \pm 0.05\ \mu F\,cm^{-2}$). In literature, C_H has been evaluated between 3.5 and $8\ \mu F\,cm^{-2}$ for n-Si [18]. Since the measured capacitance accounts for C_H and C_{sc} in series, C is given by Eq. 5:

$$\frac{1}{C} = \frac{1}{C_H} + \frac{1}{C_{sc}} \tag{5}$$

$$C_{sc} = \left(\frac{\epsilon\epsilon_o e N_D}{2}\right)^{\frac{1}{2}} \cdot (U - U_{fb})^{-\frac{1}{2}} \tag{6}$$

Using Eq. 5, with C calculated from Fig. 4a and with $C_H = 5\ \mu F\,cm^{-2}$, one found $C_{sc} = 0.55 \pm 0.06\ \mu F\,cm^{-2}$. This value is in agreement with the Mott–Schottky equation (Eq. 6) that gives the capacitance of the SCL in the same range ($C_{sc} = 0.3\ \mu F\,cm^{-2}$). According to Eq. 5, the interfacial capacitance depends on C_{sc} that varies with the applied voltage (Eq. 6). Thus, C must decrease when the sample is reverse biased ($U - U_{fb} > 0$). Since the current density is proportional to C (Eq. 3), $|j|$ decreases from −0.06 to 0.14 V. This explains why the voltammograms shown in Fig. 3c exhibit a trapezoid shape instead of a regular rectangle.

Capacitance measurements

Capacitance measurements by ac-electrochemical techniques have been used to investigate the charge distribution at the interface. Figure 5 shows the evolution of

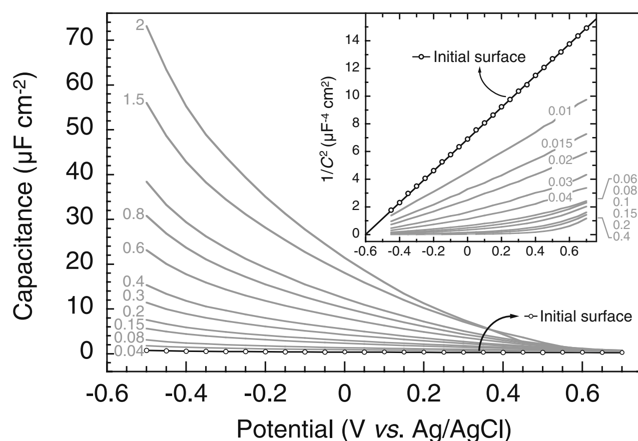

Fig. 5 Evolution of C vs U during the porous etching (Q is indicated on the plot in coulombs per square centimeter). *Inset*: Mott–Schottky representation on the same potential range (Q is indicated on the plot in coulombs per square centimeter)

the interfacial capacitance during the dissolution and the inset gives the Mott–Schottky representation. For the intact surface, $\frac{1}{C^2}$ exhibits the typical linear behavior of a depleted semiconductor (described by Eq. 6) and the extrapolated flat band potential ($U_{fb} = -0.6$ V) corresponds to the expected value for n-InP at pH = 0. The doping concentration is calculated from the slope ($N_D \approx 10^{18}$ at per cubic centimeter) in agreement with the wafer manufacturer specifications.

As seen by voltammetry in the previous section, the C vs U curves show, again, a steep increase of the interfacial capacitance during the pore growth. This variation is peculiarly strong for low reverse bias, while C tends to similar values for the highest potentials. The corresponding evolution, i.e., decrease of $\frac{1}{C^2}$ for low reverse bias while the drop is less intense for the highest potentials, is observed on the Mott–Schottky representation (see inset of Fig. 5). Note that each graph type emphasizes the capacitance response for a different range of the anodic charge. In order to explain such evolution, the specific geometry of the SCL within the porous structure has to be considered. As proposed by Erné et al. [15], for low reverse bias ($W < \frac{1}{2}t_p$), the SCL is thin. It follows the electrode topography and, thus, it increases linearly with the geometric area (A_p). For sufficiently high polarization, the SCL is thick ($W \geq \frac{1}{2}t_p$); two opposite SCL overlap in each nanowall. C_{sc} is much less dependent on A_p and the electroactive area of the sample tends to recover its initial value (i.e., the pore tips). Such a phenomenon is visible on the Mott–Schottky plots. A curvature of $\frac{1}{C^2}$ vs U starting at ca. 0.2 V (i.e., $U - U_{fb} = 0.8$ V) is indeed observed since $2 \times W$ is in the range of the pore wall thickness ($W = 40$ nm and $t_p = 50$ to 100 nm). Similar observations have been reported in literature on both SiC and GaP [14, 15].

Photoelectrochemical properties

Figure 3b presents the voltammogram obtained under white light illumination for the initial flat surface (black line). The typical photoelectrochemical behavior for n-type InP is observed. An anodic photocurrent is measured when the sample is reverse-biased while no effect of the light is detected on the cathodic current. The photocurrent threshold (U_{ph}) located around 0 V is followed by a current plateau until 0.6 V, where the onset of the anodic current in the dark is attained (see Fig. 3a). The photocurrent plateau indicates that the system has reached its maximum quantum yield. The evolution of the photovoltammogram with the porous etching is also shown in Fig. 3b (colored lines). When the anodic charge is increased, the photocurrent thresh-

old remains unchanged. This is in line with the Mott–Schottky analyses that have shown no variation of U_{fb}. Conversely, the photocurrent plateau decreases with the porous etching. This result is surprising since, according to Erné et al. [15], the light scattering within the porous layer should increase the absorption of photons and, thus, the photoconversion efficiency.

Figure 6 shows the variation of the photocurrent spectrum during the pore growth. The spectra are carried out at $U = 0.6$ V, which corresponds to the photocurrent plateau observed in Fig. 3. The empty circles correspond to the spectrum of the initial flat InP surface. As expected, the photocurrent is roughly constant for $600 < \lambda < 800$ nm, and it drops for $\lambda > 800$ nm since the excitation energy becomes lower than the energy band gap of the semiconductor (at $T = 298$ K, $E_g = 1.35$ eV, i.e., $\lambda = 920$ nm). When the porous etching is initiated, the photocurrent spectra are significantly modified.

For anodic charges lower than $0.5\,\mathrm{C\,cm^{-2}}$, an homogeneous increase of the current is observed with a simultaneous redshift of the spectrum edge (black full line). According to the normalized spectra, the initial j_{ph} increase is not λ-dependent. Such a phenomenon has been observed on II–VI semiconductors [19, 20], and it has been attributed to a surface roughening inducing a reflectivity decrease or a removal of recombination centers at the surface during the etching process. The redshift is approximatively equal to 20 meV. It can be ascribed to the creation or to the enhancement (related to A_p expansion) of surface states within the band gap close to the conduction or the valence band.

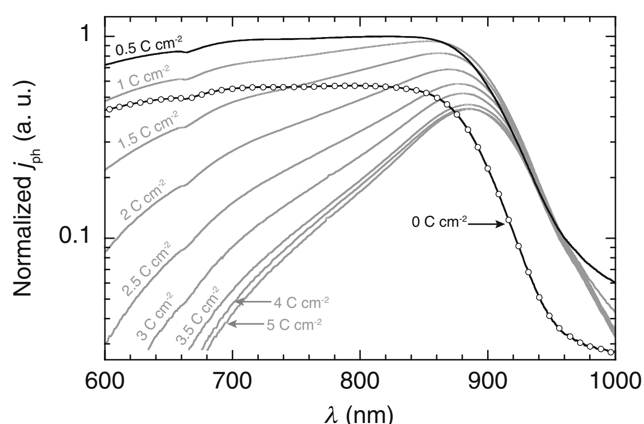

Fig. 6 Evolution of photocurrent spectra during porous etching of n-InP in 1 M HCl at $100\,\mathrm{mA\,cm^{-2}}$. Spectra are obtained at 0.6 V vs Ag/AgCl. *Empty circles* and the *black line* correspond to the initial surface and after passing $0.5\,\mathrm{C\,cm^{-2}}$, respectively. The following *gray lines* are performed after passing higher anodic charges as indicated in the figure

It has been previously proposed that electron injection via surface states located close to the conduction band could occur during InP photodissolution. These additional states could originate from adsorbed corrosion products [21]. A redshift of the low T photoluminescence of porous n-InP has also been attributed to a surface state continuum located below the conduction band edge [9].

As seen in Fig. 6, for higher anodic charges ($Q > 0.5\,\mathrm{C\,cm^{-2}}$), j_{ph} drops non-uniformly and progressively. Such spectacular variations have been previously observed on porous CdZnTe, and a model based on the variation of both absorption coefficient (α) and optical path length (x) inside the porous structure has been proposed [17]. In the porous layer, light travels partly through the material and partly through the electrolyte. According to the effective medium theory, the light travels straightforwardly through the film and an effective absorption coefficient (α_p) that accounts for the porosity has to be defined. However, this description does not correspond to the physical situation. Due to optical scattering, light reaches the bulk semiconductor after an optical path length much longer than the thickness of the porous layer [15, 22] and absorption results from the optical path length inside the pore walls. As mentioned before, due to the confinement in the nanowalls, for sufficiently high bias, an overlapping of the SCLs proceeds at these locations. This leads to establishing a lower electric field within the walls as compared to a flat semiconductor surface. The potential within the SCL (U_{sc}) for a semiconductor comes from the integration of the Poisson's equation [23]. According to Eq. 7, it is equal to $U - U_{fb}$.

$$U_{sc} = \frac{eN_D}{2\epsilon\epsilon_\circ} \cdot W^2 \quad \text{when} \quad W < \frac{1}{2}\, t_p, \tag{7}$$

In the case of the porous material, U_{sc} is also described by Eq. 7 until $W < \frac{1}{2}\, t_p$. However, for a sufficiently high reverse bias, $W \geq \frac{1}{2}\, t_p$, one has to consider the specific geometry of the nanowalls and, thus, the overlapping of the facing SCLs. Similarly to ZnO and GaN nanowires [24, 25], Eq. 8 applies in this specific case.

$$U_{sc} = \frac{eN_D}{2\epsilon\epsilon_\circ} \cdot \frac{t_p^2}{4} \qquad \text{when} \quad W \geq \frac{1}{2}\, t_p \tag{8}$$

Hence, conversely to the intact InP, the band bending within the pore walls depends also on the morphology (i.e., t_p) and not solely on the applied voltage (i.e., $U - U_{fb}$). Using these equations for $U - U_{fb} = 1.2$ V, $N_D = 10^{18}\,\mathrm{cm^{-3}}$, $W = 40$ nm, and $t_p = 50$ nm, U_{sc} is 1.2 V for the flat surface, while it is only 0.45 V in the pore walls. Since the electric field is the driving force

to separate charge carriers, the model assumes that no charge separation occurs in the porous film. This layer acts, therefore, as a photoelectrically "dead" layer (i.e., an absorbent film) [26, 27]. In the layer, the photogenerated carriers recombine radiatively or not. In order to get an efficient photoconversion, photons have to reach a region exhibiting a depth equal to $W + L$ (L, the h^+ diffusion length) situated below the pore tips ($x \geq d_p$). Using such an approach, for a defined λ, the photocurrent can be written as follows:

$$\frac{j_{ph}}{e\phi^\circ} = \exp(-\alpha_p \cdot d_p) \cdot \left[1 - \frac{\exp(-\alpha W)}{1 + \alpha L}\right], \quad (9)$$

where e and ϕ° are the elementary electric charge and the incident light flux, respectively. The first term of Eq. 9 accounts for the porous layer that acts as an optical filter, while the second corresponds to Gärtner's photocurrent response of a semiconductor [28]. When d_p increases, an exponential decay of j_{ph} occurs. The evolution of the photocurrent response during the pore growth has been simulated using Eq. 9. The absorption coefficient of the material is taken from literature [29]. Since the absorption is correlated to the material density, α_p should be lower than α. According to a previous work, where porous InP is characterized by photoluminescence measurements [11], $\alpha_p = 0.25 \times \alpha$. The calculated spectra are plotted in Fig. 7. Their evolution exhibits a relatively good agreement with the experimental data shown in Fig. 6. It confirms, therefore, the absorbent properties of the porous layer exhibiting a lower α since the film is less dense. However, a discrepancy between the experimental and the calculated spectra appears progressively. The decay of the experimental j_{ph} slows down with the anodic charge, while the simulation does not. The oversimplified description of the porous film as a photoelectrical "dead" layer, where no charge recombination occurs, cannot totally describe the evolution of the photocurrent response during the etching of the surface. In addition, the model does not describe the entire process. Obviously, it renders neither the initial current increase nor the redshift of the absorption edge.

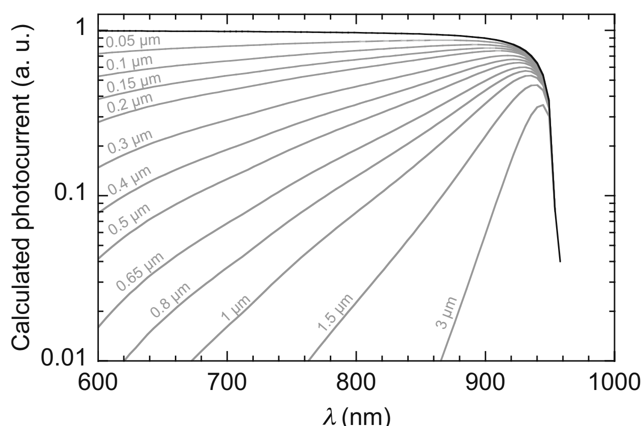

Fig. 7 Calculated photocurrent spectra for increasing pore depth (d_p are indicated on the plot). The parameters are: $U = 0.6\,\text{V}$ ($W = 40\,\text{nm}$), $L = 2\,\mu\text{m}$, and $\alpha_p = 0.25 \times \alpha$

Conclusion

SEM examinations have shown the pore morphology corresponds to the expected CLO geometry. Some crystallographic etching features are, nevertheless, visible since the applied current is not sufficiently high. The pore depth is found proportional to the anodic charge.

As reported in the literature, most of the properties' modifications observed after the pore formation can be related to the specific geometry of the structures. Both cyclic voltammetry and capacitance measurements show that the current and the capacitance are apparently enhanced because the electroactive area is increased during the porous etching. The Mott–Schottky analysis indicates additionally that, for a sufficiently high reverse bias, the porous layer is fully depleted. It is noteworthy to mention that both U_{fb} and U_{ph} remain unchanged during the pore formation. It indicates that, although the macroscopic responses of the nanostructured InP are modified, the intrinsic properties of the sample are not changed. These modifications are thus caused solely by the morphology of the nanowalls.

Similarly, the modifications of the photoelectrochemical properties are directly related to the electrode topography. (1) The initial increase of j_{ph} is attributed to a surface roughening or a removal of the recombination centers. (2) The photocurrent decrease for anodic charges higher than $0.5\,\text{C}\,\text{cm}^{-2}$ is ascribed to the photoelectrical "dead" layer behavior of the porous film due to the weak separation ability of the SCL within the nanowalls. For sufficiently high reverse bias, the potential within the pore wall depends solely on t_p. Although this approach is supported by similar results in literature and a qualitative agreement between the experimental and simulated spectra, the simplistic model requires some refinements (some charge recombinations should proceed in the porous layer).

Acknowledgements The authors are indebted to Dr. Fouad Maroun (Ecole Polytechnique—CNRS) for SEM obsevations. Dr. Nathalie Simon (Université de Versailles Saint Quentin - CNRS) is kindly acknowledged for helpful discussions about concepts of semiconductors' electrochemistry.

References

1. Santinacci L, Djenizian T (2008) C R Chimie 11:964–983
2. Kohl PA, Wolowodiuk C, Ostermayer FH Jr (1983) J Electrochem Soc 130:2288–2293
3. Takizawa T, Arai S, Nakahara M (1994) Jpn J Appl Phys 33:L643–L645
4. Foll H, Langa S, Carstensen J, Christophersen M, Tiginyanu IM (2003) Adv Mater 15:183–198
5. Langa S, Tiginyanu IM, Carstensen J, Christophersen M, Foll H (2000) Electrochem Solid-State Lett 3:514–516
6. Langa S, Carstensen J, Tiginyanu IM, Christophersen M, Foll H (2001) Electrochem Solid-State Lett 4:G50–G52
7. Langa S, Tiginyanu IM, Carstensen J, Christophersen M, Foll H (2003) Appl Phys Lett 82:278–280
8. Schmuki P, Santinacci L, Djenizian T, Lockwood DJ (2000) Phys Status Solidi A 182:51–61
9. Fujikura H, Liu AM, Hamamatsu A, Sato T, Hasegawa H (2000) Jpn J Appl Phys 39:4616–4620
10. O'Dwyer C, Buckley DN, Sutton D, Newcomb SB (2006) J Electrochem Soc 153:G1039
11. Goncalves AM, Santinacci L, Eb A, Gerard I, Mathieu C, Etcheberry A (2007) Electrochem Solid-State Lett 10: D35–D37
12. Ulin VP, Konnikov SG (2007) Semiconductors 41:832–844
13. Peter LM, Riley DJ, Wielgosz RI (1995) Appl Phys Lett 66:2355–2357
14. Konstantinov AO, Harris CI, Janzen E (1994) Appl Phys Lett 65:2699–2701
15. Erne BH, Vanmaekelbergh D, Kelly JJ (1996) J Electrochem Soc 143:305–314
16. van de Lagemaat J, Plakman M, Vanmaekelbergh D, Kelly JJ (1996) Appl Phys Lett 69:2246–2248
17. Erne BH, Mathieu C, Vigneron J, Million A, Etcheberry A (2000) J Electrochem Soc 147:3759–3767
18. Allongue P, Chazalviel JN, Henry de Villeneuve C, Ozanam F (2007) J Phys Chem C 111:5497–5499
19. Tenne R, Hodes G (1980) Appl Phys Lett 37:428–430
20. Tenne R (1983) Appl Phys Lett 43:201–203
21. Jaume J, Debiemme-Chouvy C, Vigneron J, Herlem M, Khoumri EM, Sculfort JL, Le Roy D, Etcheberry A (1994) J Phys III 4:273–291
22. Schuurmans FJP, Vanmaekelbergh D, van de Lagemaat J, Lagendijk A (1999) Science 284:141–143
23. Morrison SR (1980) Electrochemistry at semiconductor and oxidized metal electrodes. Plenum, New York
24. Mora-Sero I, Fabregat-Santiago F, Denier B, Bisquert J, Tena-Zaera R, Elias J, Levy-Clement C (2006) App Phys Lett 89:203117 (3pp)
25. Cavallini A, Polenta L, Rossi M, Stoica T, Calarco R, Meijers R, Richter T, Luth H (2007) Nano Lett 7:2166–2170
26. Wittry DB, Kyser DF (1967) J Appl Phys 38:375–382
27. Langmann U (1973) Appl Phys 1:219–221
28. Gärtner WW (1959) Phys Rev 116:84–87
29. Aspnes DE, Studna AA (1983) Phys Rev B 27:985–1009